sciendo

ISSN 1335-8871

MEASUREMENT SCIENCE REVIEW

Journal homepage: https://content.sciendo.com

Adaptive Proportional Derivative Control for Magnetic Bearing in Full Maglev Left Ventricular Assist Device

Wenfei Tao*, Chen Chen, Kejia Zhang

Artificial Organ Technology Laboratory, School of Mechanical and Electrical Engineering, Soochow University, Suzhou 215000, China, taowenfeitt@163.com

Abstract: In this paper, adaptive proportional derivative (APD) parameter control was proposed to solve the problem of high power consumption caused by the unclear mechanism of liquid disturbance during the lifting-up of magnetic bearing in left ventricular assist devices. A mathematical model was derived that describes how the rotor operates in liquid filling. The disturbance caused by the liquid in the lifting-up process was analyzed, and an adaptive control system was developed to improve dynamic performance and reduce power consumption. The experimental results show that APD control requires a shorter rise time without overshoot of rotor displacement compared to traditional fixed configurations. When using the APD controller, the peak current dropped by 8%. The duration in which the current is greater than 1A was reduced by 10.2 ms, and the average current also dropped by 34%.

Keywords: Adaptive proportional derivative control, left ventricular assist device, lifting-up power, magnetic bearing, rotor displacement measurement.

1. INTRODUCTION

Due to their good blood compatibility, magnetic bearings are commonly used in left ventricular assist devices (LVADs). In recent years, hybrid magnetic bearings (HMBs) have been used in LVADs, combining permanent magnets and electromagnets to reduce bearing dimensions and power consumption [1]-[3]. Due to the high remanence and coercivity of rare-earth magnetic materials, magnetic bearings can be designed as high-stiffness support systems. The bias magnetic field generated by a permanent magnet can significantly reduce the power consumption of magnetic bearings. Fully maglev LVADs are used as long-term implantable medical devices. A rotor requires strong support to ensure the basic quality of life of the user, which requires high robustness and high stiffness of the magnetic bearing against vibrations and shocks, as well as low power consumption and low heating.

Magnetic bearings are highly intersecting devices that combine machinery, electronics, and control. The performance of a magnetic suspension system is directly related to the performance of the control system. Magnetic bearings are unstable systems that exhibit strong nonlinearity and uncertain disturbance. To solve the problems caused by these characteristics and improve the performance, many scholars have studied advanced nonlinear control. Jeng et al. [4] used a nonlinear adaptive inverse control with a Chebyshev polynomial-based model for a magnetic bearing. Their architecture provided greater flexibility, robustness to disturbances, and a control error within ±0.015 mm. Betschon et al. [5] proposed a new method to reduce the current of an active magnetic bearing (AMB) at synchronous speeds in a wide range of rotational speeds. The matrix calculation was optimized using a linearly dependent function to minimize the computational power and memory requirements of the control system hardware. The simulation results showed that the maximum peak-to-peak current was drastically reduced by more than 50%. Basaran et al. [6] used a Lyapunov function based on composite adaptive output feedback control for a flywheel system. The position tracking errors obtained with the integral square were compared between the composite and the standard adaptive controller. At 30000 and 45000 rpm, the position tracking error dropped sharply with the composite adaptive controller compared with the standard adaptive controller. Su et al. [7] assembled proportional integral derivative (PID) controllers with two input types and a robust sliding mode control method that was used for both nonlinear and linear control systems. The newly proposed method tracked the sinusoidal input signal with good performance, which was significantly better than those of the other methods by Su. The average tracking error was 56% of the other methods, and the maximum tracking error was 35% of the other methods with thrust disk force. Zad et al. [8] designed a hybrid magnetic bearing approximated by a radial basis function neural network, and used sliding mode control to stabilize the magnetic bearing system. The simulations and

DOI: 10.2478/msr-2024-0018

*Corresponding author: taowenfeitt@163.com (W. Tao)

experimental results showed that superior position tracking of the rotor was achieved using their control algorithm under different operating conditions. Dhyani et al. [9] studied the application of fuzzy PID control based on moth-flame optimization for AMBs, and chose ITAE and ITAU to design the optimization problem and compare it with the responses of others. Carvalho et al. [10] proposed an adaptive neuro-fuzzy controller with optimally balanced vibration control performance and robustness. The experimental results showed that the neuro-fuzzy controller outperformed the PID controller in terms of energy efficiency and vibration attenuation. The optimal adaptive control of the magnetic suspension was presented for a rotary impeller of an artificial heart pump [11]. Huettner [12] investigated unbalanced rotor vibration by using vibration control compensation to significantly reduce the power consumption of blood pump magnetic bearings for bearingless slice motors. Based on the hybrid magnetic bearing blood pump, Ren [13] proposed a force balance point suspension method. By identifying the output signal of the power amplifier, the force balance point of the rotor was estimated and used as the suspension target position. This method reduced the power consumption of the magnetic bearing to less than 0.5 W. Pai [14] created a complete mathematical model of the magnetic bearing of the artificial heart and then developed a set of disturbance observers with a bandwidth of up to 45 Hz, from which the pulsation signals of the original heart could be extracted. Silva [15] performed feedback control tests on an axially magnetically levitated left ventricular assist device, which showed that the rotor vibrates axially at 1200 rpm with 80 μm in air and 40 μm in water, and the power consumption of the magnetic bearing is 2.8 W.

Currently, research on magnetic bearings for LVADs is still scarce and there is no reference index. The magnetic levitation closed-loop control used for LVADs is basically linear PID, which is simple and easy to debug. However, the problem of rotor lifting in liquid has not yet been studied. Fixed feedback parameters have the limitation that the rise time, overshoot, and adjustment time cannot be considered simultaneously, resulting in a significant increase in instantaneous power consumption during the lifting-up process, especially in the presence of an unknown disturbance. Furthermore, inappropriate parameter configuration leads to unusable electronic peripheral hardware. Although advanced adaptive parameter adjustment methods such as neural networks and fuzzy control have long been proven to be powerful and effective for solving these problems, their complex algorithms and membership function computation require extremely high computational power. For implantable medical devices, lower power consumption, higher reliability, and smaller size are key to achieving good performance. Therefore, a microprocessor chip with high computing power and high power consumption is unsuitable for implantable medical devices.

In this study, we focused on modeling a rotor operating in a liquid-filled environment and derived the stability conditions of the feedback parameter. The influence of the fluid on the rotor during the transient lifting-up was also investigated. Based on the empirical theory and the performance of the feedback parameters, adaptive proportional derivative (APD) parameter control was proposed. A two-stage piecewise linear approximation (PLA) was adopted for magnetic bearings in LVADs, which comprehensively improves the dynamic regulation performance and reduces the input requirements. By using integer arithmetic, the required computational power of the processing chip is reduced, so that the miniaturized full-maglev LVADs fit better.

2. MATHEMATICAL MODEL OF ROTOR IN LIQUID NEAR THE CENTER

Fig. 1(a) illustrates the profile of the magnetic bearing, the titanium alloy layers on the stator and rotor surfaces are not shown. In Fig. 1, the gap between the stator and rotor is magnified to show the details of the structure. Two axially magnetized permanent magnet rings were assembled independently in the stator and rotor, providing negative radial stiffness and positive axial stiffness of the rotor. The permanent magnets provided a radially biased flux, while electromagnetic coils were used for active control. When the rotor deviates from the set position, the displacement sensor feeds the rotor information to the controller, which generates the control signal required to drive the electromagnetic coils. Subsequently, the rotor is pulled back to the preset target position. Since the rotors of the LVADs were completely immersed in blood, they were also exposed to the force of the fluid.

The magnetic energy can be expressed as

$$W_m = \iint BdHdV, \tag{1}$$

where B is the magnetic flux density, H is the magnetic field intensity, and V is the volume of the field. According to the principle of virtual displacement, the magnetic force is

$$F_m = \frac{\partial W_m}{\partial X} = \frac{\partial \iint BdHdV}{\partial X}, \tag{2}$$

where X denotes the displacement under generalized degrees of freedom.

Using the x-axis as an example and considering that the rotor is near the center point, the magnetic flux leakage without an iron core and the curvature of the rotor and stator were ignored. The effect of the differential magnetic radial force on the rotor through each of the magnetic poles can be written as

$$F_{mag} = \frac{(B_0+B_x-B_c)^2-(B_0-B_x+B_c)^2}{\mu_0} S = \frac{4S}{\mu_0}(B_0B_x - B_0B_c), \tag{3}$$

where B_0 is the radial bias magnetic flux density provided by the permanent magnets, B_x is the magnetic flux density of the permanent magnet caused by the rotor displacement, B_c is the electromagnetic flux density generated by the coils (electromagnets), μ_0 is the vacuum permeability, and S is the surface area of the magnetic poles. The permanent magnet flux caused by the rotor displacement can be calculated approximately as

$$B_x \approx k_m x\,, \tag{4}$$

where k_m refers to the permanent-displacement gain coefficient and x corresponds to the rotor displacement in the x-direction.

According to Maxwell's loop theorem,

$$\oint H_x dl = Ni_x, \tag{5}$$

where l contains the length of the entire loop. If the reluctance of the magnetic permeability material is ignored, the electromagnetic flux generated by the coils in the gap can be expressed as

$$B_c = \frac{\mu_0 N i_x}{2x_c}, \tag{6}$$

where N is the number of turns in the electromagnetic coils, i_x is the current of the electromagnetic coils in the x-direction, and x_c corresponds to the gap.

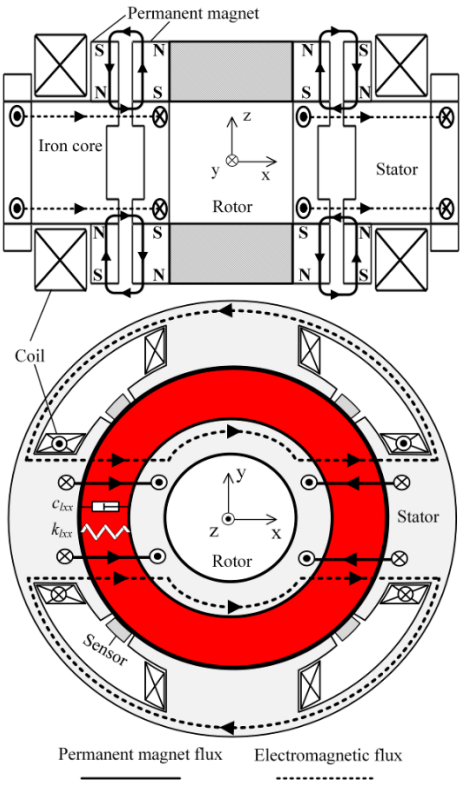

(a)

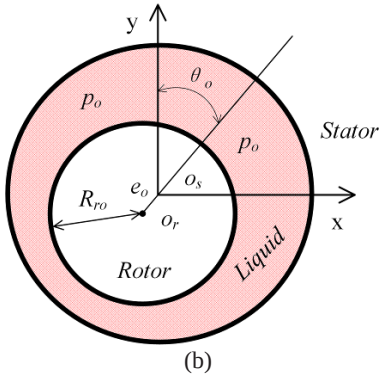

(b)

Fig. 1. (a) Radial and axial diagrams of the magnetic bearing, (b) Schematic of the rotor in a liquid-filled environment.

After substituting (4) and (6) into (3), the magnetic force near the center point ($x = 0, i_x = 0$) can be expressed using a Taylor series expansion as follows:

$$F_{mag} = k_x x - k_i i_x, \tag{7}$$

where

$$k_x = \frac{4B_0 S k_m}{\mu_0}, \tag{8}$$

$$k_i = \frac{2B_0 SN}{x_c}. \tag{9}$$

k_x is the force-displacement coefficient in the x-direction, and k_i is the force-current coefficient. In the case of partial nonlinearity in the iron core, these two coefficients change partially, and the system exhibits strong nonlinear characteristics with parameter perturbations.

Fig. 1(b) shows a schematic of the rotor in a liquid-filled environment. When the rotor rotates at a constant angular frequency, the rotor whirls within a small range, and the entire system is in a steady state. The point o_r corresponds to the center of the rotor, the point o_s is the center of the stator, and e_o indicates the eccentricity. The angle θ_o between the two center points and the y-axis of the stator coordinate system is the eccentricity angle. The radius of the rotor is R_{ro}, and the axial height of the rotor is H_r. Moreover, p_o denotes the pressure distribution, which is a function of position.

Accordingly, the fluid force acting on the rotor can be expressed as

$$\begin{cases} F_{lx} = \int_{-H_r/2}^{H_r/2} \int_0^{2\pi} -p_o \sin\theta_o \, R_{ro} d\theta_o dz \\ F_{ly} = \int_{-H_r/2}^{H_r/2} \int_0^{2\pi} -p_o \cos\theta_o \, R_{ro} d\theta_o dz \end{cases}. \tag{10}$$

Equation (10) can be expanded as eight parameters near the center point:

$$k_{lxx} = \left.\frac{\partial F_{lx}}{\partial x}\right|_{x=x_e,\ y=y_e},\ k_{lxy} = \left.\frac{\partial F_{lx}}{\partial y}\right|_{x=x_e,\ y=y_e}$$

$$c_{lxx} = \left.\frac{\partial F_{lx}}{\partial \dot{x}}\right|_{x=x_e, y=y_e}, c_{lxy} = \left.\frac{\partial F_{lx}}{\partial \dot{y}}\right|_{x=x_e,\ y=y_e}$$

$$k_{lyy} = \left.\frac{\partial F_{ly}}{\partial y}\right|_{x=x_e, y=y_e}, k_{lyx} = \left.\frac{\partial F_{ly}}{\partial x}\right|_{x=x_e,\ y=y_e}$$

$$c_{lyy} = \left.\frac{\partial F_{ly}}{\partial \dot{y}}\right|_{x=x_e, y=y_e}, c_{lyx} = \left.\frac{\partial F_{ly}}{\partial \dot{x}}\right|_{x=x_e,\ y=y_e},$$

where $x = x_e, y = y_e$ is the static operating point of the rotor (center point) and $\dot{x}$ and $\dot{y}$ are the derivatives of the rotor displacement with respect to time (rotor radial velocity). These eight parameters represent the stiffness and damping coefficients in their respective directions and cross directions and they are closely related to the rotational speed of the rotor. The stiffness coefficients of the active magnetic bearing are much higher than those caused by the fluid, and the fluid stiffness coefficient matrix can be completely ignored. However, the magnetic bearing itself is an undamped system, and the damping force of the fluid cannot be ignored (unless the feedback damping is much larger than the liquid damping, but this is often difficult to achieve).

Thus, the impact of the liquid force on the rotor in the x-direction can be written as

$$F_{lx} = -c_{lx}\dot{x}. \tag{11}$$

To unify the symbols of the parameters of the dynamic system, $c_{lx} = \left|c_{lxx} + c_{lyx}\right|$ stands for the damping coefficient of the liquid force in the x-direction. In general, the damping force of the fluid dissipates excess rotor energy and the cross-damping coefficient has little effect. These two parameters are strongly related to the liquid and the rotational speed of the rotor are difficult to calculate and measure.

Then, the mechanical equilibrium equations in the x- and y-directions can be calculated as

$$\begin{cases} \hat{m}\ddot{x} = k_x x - k_i i_x - c_{lx}\dot{x} \\ \hat{m}\ddot{y} = k_y y - k_i i_y - c_{ly}\dot{y} \end{cases}, \tag{12}$$

where $\ddot{x}\ and\ \ddot{y}$ are the rotor acceleration in the x- and y-directions, respectively, k_y is the force-displacement coefficient in the y-direction, i_y is the current of the electromagnetic coils in the y-direction, c_{ly} is the damping coefficient of the liquid force in the y-direction, m is the rotor mass, and $\hat{m}$ is the equivalent mass of the rotor (which contains the mass of the liquid attached to the rotor surface). The equivalent mass of the rotor is difficult to estimate and measure.

3. STABILITY OF MAGNETIC BEARING

A voltage-controlled power amplifier was used to control the electromagnetic coils, which increased the efficiency of the power devices. A voltage-controlled magnetic bearing has a higher order than a current-controlled bearing. Third-order voltage control is more robust than second-order current control; however, it requires consideration of the inductance and resistance in the magnetic bearing system as well as the systematic stability and properties.

Since the main magnetic flux of the permanent magnet does not flow through the electromagnetic coils and the position change of the rotor does not cause variable inductance of the electromagnets, the back electromotive force can be completely ignored. If the voltage of the coils is considered as input, the voltage can be written as

$$u = iR + L\frac{di}{dt}, \tag{13}$$

where R is the resistance of the electromagnet, L is the inductance of the electromagnet, and u is the voltage of the electromagnet (input). With respect to the critical mechanical frequency bands of the rotor considered in this study, the inductance and resistance of the electromagnetic coils can be considered constant.

Table 1 lists the mechanical and electrical parameters of the magnetic bearing system. The force-displacement coefficient and the force-current coefficient were measured based on the stiffness test platform (not discussed in this paper). The inductance and resistance of the electromagnets were measured using an impedance analyzer. In the critical mechanical frequency range of 500 Hz, the inductance and resistance of the electromagnetic coils varied slightly and were considered constant.

Table 1. Magnetic bearing parameters.

Parameter	Unit	Numerical value
k_x and k_y	N/m	66000
k_i	N/A	6.8
R	Ω	4.5
L	mH	2.2

Since the two axes are symmetrical, the x-axis is analyzed as an example. After differentiating (12) gain with respect to time, the derivative of the current with respect to time can be expressed as

$$\frac{di_x}{dt} = \frac{k_x\dot{x} - c_{lx}\ddot{x} - \hat{m}\dddot{x}}{k_i}. \tag{14}$$

Substituting (12) and (14) into (13), the mathematical model of the voltage-controlled magnetic bearing can be written as

$$-\frac{L\hat{m}}{k_i}\dddot{x} - \frac{Lc_{lx} + R\hat{m}}{k_i}\ddot{x} + \frac{Lk_x - Rc_{lx}}{k_i}\dot{x} + \frac{k_x R}{k_i}x = u\,. \tag{15}$$

Equation (15) shows that the voltage-controlled magnetic bearing is a third-order dynamic system that cannot be reduced. The above quantitative model-based differential equation operation can be used to obtain the standard state-space model of the system directly without using the Lie derivative.

Based on (15), the state-space model can be calculated simultaneously as

$$\begin{cases} \dot{x}_1 = x_2 \\ \dot{x}_2 = x_3 \\ \dot{x}_3 = \frac{k_x R}{L\hat{m}}x_1 + \left(\frac{k_x}{\hat{m}} - \frac{c_{lx}R}{L\hat{m}}\right)x_2 - \left(\frac{R}{L} + \frac{c_{lx}}{\hat{m}}\right)x_3 - \frac{k_i}{L\hat{m}}u \\ x_{out} = x_1 \end{cases}, \tag{16}$$

where x_1, x_2, and x_3 denote the displacement, velocity, and acceleration of the rotor, respectively. Its matrix form can be expressed as

$$\dot{\boldsymbol{X}} = \boldsymbol{A_l X} + \boldsymbol{B}u\,, \tag{17}$$

where

$$\boldsymbol{A_l} = \begin{bmatrix} 0 & 1 & 0 \\ 0 & 0 & 1 \\ \frac{k_x R}{L\hat{m}} & \frac{Lk_x - c_{lx}R}{L\hat{m}} & -\left(\frac{R}{L} + \frac{c_{lx}}{\hat{m}}\right) \end{bmatrix}, \quad \boldsymbol{B} = \begin{bmatrix} 0 \\ 0 \\ \frac{-k_i}{L\hat{m}} \end{bmatrix}.$$

The system input can then be configured as

$$u = \boldsymbol{KX} = [K_P \quad K_D \quad 0][x_1 \quad x_2 \quad x_3]^{\mathrm{T}} = K_P x_1 + K_D x_2\,, \tag{18}$$

where K_P and K_D denote the feedback stiffness and damping after amplification by the power amplifier and k_P and k_D denote the feedback stiffness and damping of the controller configuration. The relationship between these two sets of parameters can be considered as direct amplification. Note that the speed signal of the rotor is obtained by differentiating the collected displacement sensor signals, followed by a digital low-pass filter to filter the noise of the displacement sensors. Therefore, the radial velocity signal of the rotor can be considered as a measurement signal.

Once the parameters have been introduced in (17), the matrix can be calculated as

$$\boldsymbol{A_l + BK} = \begin{bmatrix} 0 & 1 & 0 \\ 0 & 0 & 1 \\ \frac{k_x R - K_P k_i}{L\hat{m}} & \frac{Lk_x - c_{lx}R - K_D k_i}{L\hat{m}} & -(\frac{R}{L} + \frac{c_{lx}}{\hat{m}}) \end{bmatrix}. \quad (19)$$

Then the system can be expressed as

$$\dot{\boldsymbol{X}} = (\boldsymbol{A_l + BK})\boldsymbol{X}.$$

The real part of the eigenvalues λ_i in the matrix $\boldsymbol{A_l + BK}$ must be less than 0, which ensures the convergence of the system. The feedback parameters must then be guaranteed as

$$\begin{cases} K_P > k_x R/k_i \\ K_D > (Lk_x - c_{lx}R)/k_i \end{cases}. \quad (20)$$

The damping coefficient of the liquid improves the stability margin of the system when the rotor is at the center. The liquid attached to the surface of the rotor increases the rotor mass, and the bandwidth of the system decreases significantly, which loosens the requirements on the measurement and control system. Consequently, the performance requirements for the processing chip and the bandwidth of the displacement sensor are reduced.

The closed-loop system of the magnetic bearing is usually designed with a mathematical model near the center point of the rotor, but the entire transient lifting-up process must be refined when the rotor is filled with liquid. At this stage, the fluid force can be considered as an unknown disturbance. The mathematical modeling in this part is difficult, but the entire physical process can be easily described.

Fig. 2 briefly shows the physical process of lifting. In the initial phase, the rotor must overcome the radial force exerted by the liquid to accelerate, and the rise time is longer than in the air. However, when the rotor slows down near the center point, the liquid moves faster than the rotor, and the liquid force is reversed to the rotor, which is manifested as an increase in overshoot.

Due to the physical process mentioned above, it is impossible to achieve favorable motion performance with linear, fixed feedback parameters.

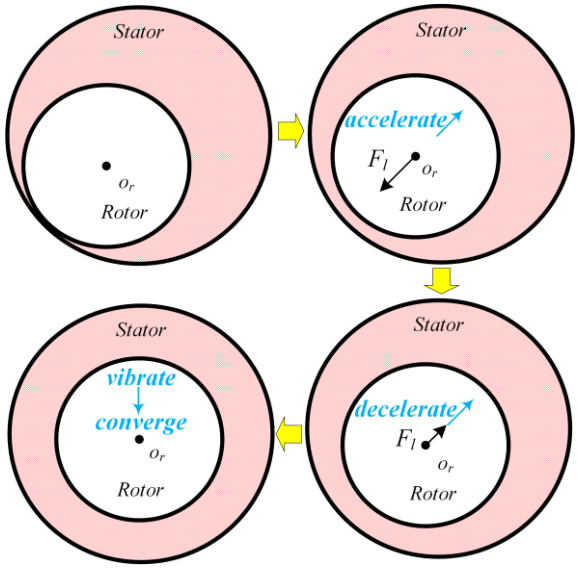

Fig. 2. Transient process of lifting.

4. APD CONTROL FOR MAGNETIC BEARING IN LVADS

The use of fixed feedback parameters has the limitation that the rise time, the overshoot, and the adjustment time cannot be considered simultaneously. Moreover, this approach is ineffective against unknown perturbations.

The adaptive rates of the parameters are based on the analysis of the above physical process. When the rotor is in the lifting-up process in the water, a large feedback stiffness and a small feedback damping away from the center point should be set to reduce the rise time. When the rotor is near the center point, the feedback stiffness should be reduced and the feedback damping increased to reduce overshoot and adjustment time.

Fig. 3 shows a block diagram of the entire control system.

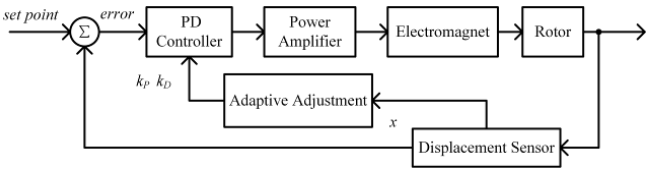

Fig. 3. APD control block.

Fig. 4 shows the adaptive parameter function of PLA and the corresponding parabola. Under ideal conditions, the system must satisfy the sufficiently smooth Lipschitz conditions. Accordingly, the parameter adjustment can be designed in the parabolic form shown in Fig. 4. The upper and lower bounds of the parameters are identified in the figure. The boundaries of the parameters in Fig. 4 must satisfy the stability condition. A sufficiently smooth parabolic arithmetic parameter implies that floating-point arithmetic should be used in the processing chip, which increases the computational power requirements (double precision must be used to ensure accuracy near the vertex of a parabola). Implantable medical devices have high requirements on product size, power consumption, and heating. In this study, we used a piecewise linear approximation method to obtain an approach that requires only integer operations.

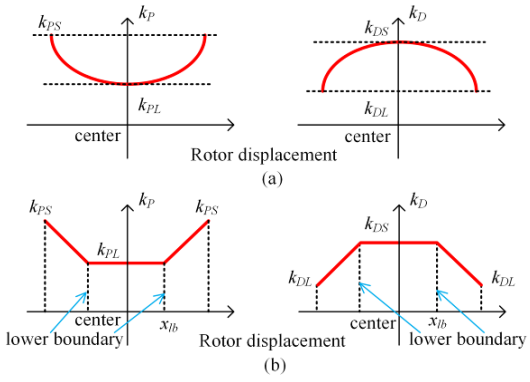

Fig. 4. Adaptive parameter function of PLA and parabola.

The error can be ignored if multiple line segments are used to approximate a parabola. Considering the bandwidth and control accuracy requirements of the magnetic-bearing system, we adopted the two-stage piecewise linear approximation shown in Fig. 4. The nearby vertex of the parabola was replaced by a constant, thus avoiding high-precision operations.

The mathematical expression of the parabola for the feedback stiffness and the feedback damping can be written as

$$\begin{cases} k_P^{Par}(x) = \alpha x^2 + \alpha_0 \\ k_D^{Par}(x) = -\beta x^2 + \beta_0 \end{cases},$$

where α, α_0, β, and β_0 are the parabolic coefficients. However, if the coefficients of the parabola are not integers, the operation near the top of the parabola must be a floating point number to ensure accuracy.

The mathematical expression of the two-stage PLA for the feedback stiffness and the feedback damping can be written as

$$k_P^{tP}(x) = \begin{cases} -\sigma_P x + \sigma_{P0}, & x < -x_{lb} \\ \gamma_P, & x_{lb} \le x \le -x_{lb} \\ \sigma_P x + \sigma_{P0}, & x > x_{lb} \end{cases}$$

$$k_D^{tP}(x) = \begin{cases} \sigma_D x + \sigma_{D0}, & x < -x_{lb} \\ \gamma_D, & x_{lb} \le x \le -x_{lb}, \\ -\sigma_D x + \sigma_{D0}, & x > x_{lb} \end{cases}$$

where $\sigma_P, \sigma_{P0}, \gamma_P, \sigma_D, \sigma_{D0}$, and γ_D are the PLA coefficients. Except for the region near x_{lb}, all regions can be derived. In the lifting-up process, this point can be quickly crossed, and the rotor subsequently vibrates near the center point. The pitch of the curve can be set to an integer, ensuring that all operations are integers within the permissible accuracy. The k_{PL} cannot fall below 80 for stability. The selection range of k_{DS} is usually large but it should not exceed 45 considering the impact of sensor noise.

5. Experiment

The center point of the displacement sensor was at 1.475 V, and the sensors adopted a differential output signal. The rotor was fixed to start in the same position by adjusting different parameters, and the signals of the displacement sensor and the output current signal of the power supply were observed. The rotor was located on one side near the displacement sensor and 45° on both sides of the x and y magnetic poles. The measured output current of the power supply included all magnetic poles. Based on the mechanical bandwidth of the magnetic bearing, the sampling rate of the displacement sensor signal was set to 5 kHz to reduce the acquisition of ineffective noise signals. The current sampling rate was set to 10 MHz to collect as much of the actual peak current as possible. The rotor was immersed in water in the test environment. The normal working gap of the rotor was 0.25 mm, and the lower boundary in Fig. 4 was set to ±0.05 mm. The corresponding feedback parameters were $k_{PS} = 120$, $k_{PL} = 110, k_{DS} = 33$, and $k_{DL} = 5$. Fig. 5 shows an image of the test setup. The oscilloscope model is Tektronix MDO3034.

Fig. 6 shows the curve of the rotor movement in air under different feedback parameters, and Fig. 7 shows the curve of the rotor movement in water under different feedback parameters.

Regardless of whether the rotor is in water or in air, with fixed feedback stiffness, the overshoot gradually decreases with increasing feedback damping, while the rise time increases only slightly. The feedback damping evidently influences the rise time to a lesser extent but correlates strongly with the overshoot and adjustment time. With fixed feedback damping, the overshoot increases with increasing feedback stiffness.

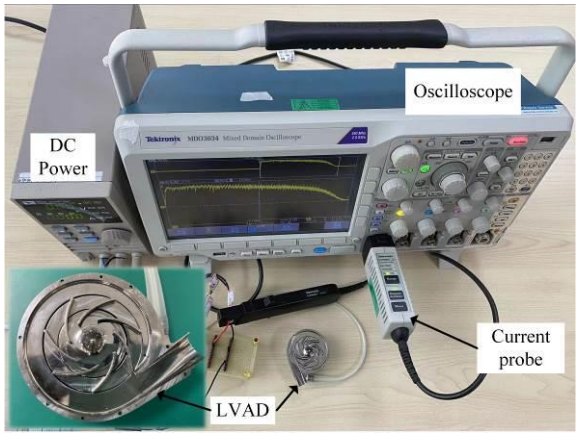

Fig. 5. Test setup.

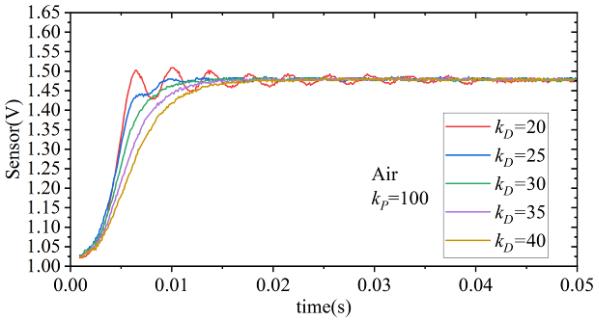

(a)

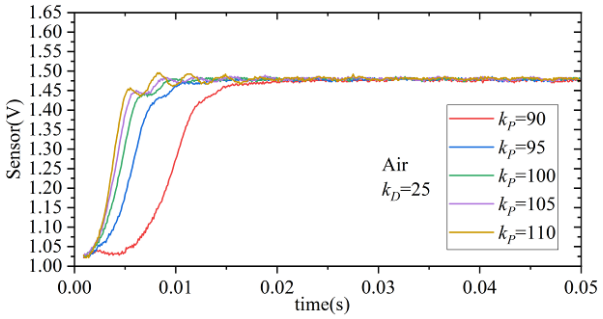

(b)

Fig. 6 (a) Displacement of rotor in air at lifting-up under constant stiffness with variable damping, (b) Displacement of rotor in air at lifting-up under constant damping with variable stiffness.

Fig. 8 shows a comparison of the performance of the rotor in air and water with the same feedback parameters. The rotor lifting in water has a longer rise time and greater overshoot than in air. The reasons for the slow response speed of the rotor in water are consistent with the analysis shown in Fig. 2. Furthermore, the rotor receives an additional force from the fluid.

Fig. 8 clearly shows that the lifting-up process cannot be explained by a center point mathematical model. The damping effect of the liquid should reduce the amount of overshoot, but this could not be achieved due to the relative motion of the liquid and the rotor.

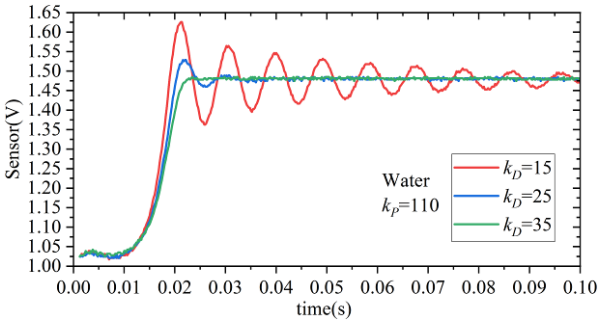

(a)

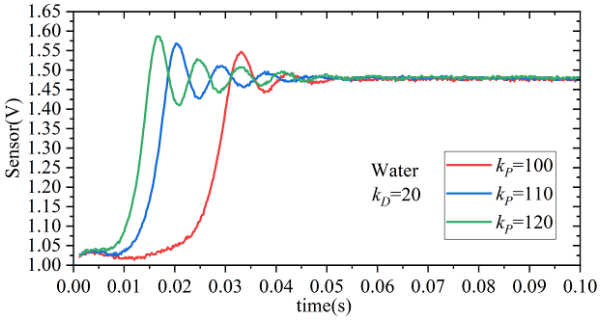

(b)

Fig. 7 (a) Ddisplacement of rotor in water at lifting-up under constant stiffness with variable damping, (b) Displacement of rotor in water at lifting-up under constant damping with variable stiffness.

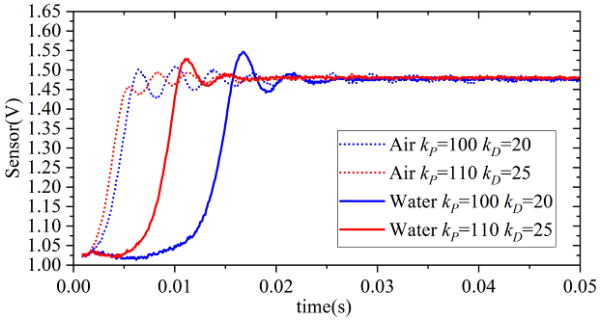

Fig. 8. Displacement of rotor at lifting-up between in air and water under the same parameters.

Fig. 9 compares the APD with the traditional fixed parameters. The APD parameters have a shorter rise time without any overshoot. Due to the flexible adjustment of the feedback parameters, the APD results show strong performance in terms of rotor movement.

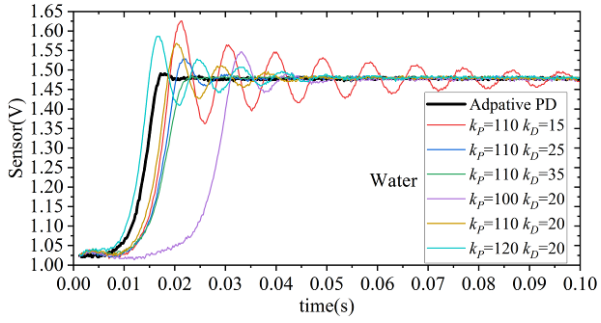

Fig. 9. Comparison of APD and fixed parameters.

Fig. 10 compares the output currents of the three sets of feedback parameters. The output current of the external power supply was measured with the current probe of an oscilloscope.

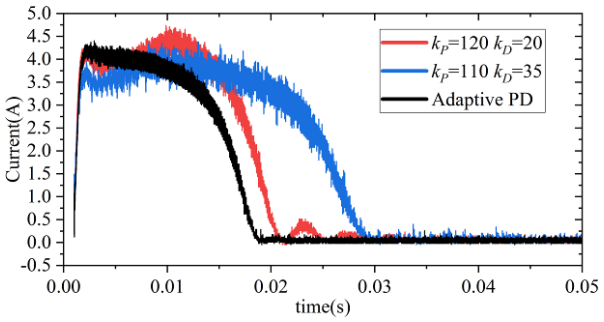

Fig. 10. Comparison of the output current of the three control methods.

Both the peak output current and the high-current-duration APD control showed large improvements compared to the other two configurations of the feedback parameters.

The output current signals for each group are shown in Table 2. The peak current of the APD is 92.8% of that of the combination of large feedback stiffness and small feedback damping. Also, the time required to reach an output current of more than 1 A is reduced by 10.2 ms compared to the combination of large feedback damping and small feedback stiffness, and the average current of 50 ms is only 66% of the maximum.

Table 2. Comparison of current with each group.

Parameter	Peak current [A]	Less than 1 A moment [ms]	50 ms average current [A]
Adaptive PD	4.40	17.1	1.19
k_P =120, k_D =20	4.74	19.5	1.44
k_P =110, k_D =35	4.38	27.3	1.81

From the current waveform in Fig. 10, it can be inferred that a larger feedback damping leads to a larger current envelope, which can be attributed to the influence of displacement sensor noise. As the rotor approaches the center point, its speed decreases and the current envelope becomes smaller.

With a large feedback damping, a digital low-pass filter with a lower cut-off frequency must be configured to reduce the influence of the displacement sensor; however, this approach generally leads to a strong hysteresis of the current.

In the laboratory environment, an STM32F1 chip (72 MHz) was selected to compare the code running times required by the integer PLA and the floating-point adaptive, and the results are shown in Table 3. If a chip that supports hardware floating-point arithmetic is selected, the running time of floating-point arithmetic can be significantly reduced; however, such chips may not be suitable for use in implantable medical devices. This is because floating-point arithmetic offers only a negligible improvement in control performance. The two-stage integer PLA is sufficient based on the output current and rotor displacement signal.

Table 3. Comparison of running time between integer and floating-point methods.

	Integer PLA adaptive	Floating-point adaptive
Running time [μs]	7.63	39.92

6. Conclusion

In this study, a mathematical model was created for the magnetic bearing system of a fully magnetic levitation LVAD in a liquid-filled environment. In addition, the stability condition was analyzed and derived, and the feedback parameters were adaptively designed for the lifting-up process. The adaptive PD control showed superior performance for magnetic bearings in LVADs than the fixed-parameter PD control. The magnetic bearings had less dependence on peripheral power components, especially in the power management section. Furthermore, the reduction in output current resulted in decreased heat loss. The two-stage integer PLA adaptive control effectively reduced computational complexity, making it more suitable for implantable medical devices that have strict requirements for volume, power, heat loss, and reliability. Finally, the average current of 50 ms dropped by 34% and the peak current dropped by 8%.

A limitation of this work is that the range selection of the adaptive parameters is not yet sufficiently intelligent, which will be the focus of further research. In the future, the problem of slow response at lifting-up, which is caused by the fluid forces, needs to be solved.

References

[1] Chen, C., Paden, B., Antaki, J., Ludlow, J., Paden, D., Crowson, R., Bearnson, G. (2002). A magnetic suspension theory and its application to the HeartQuest ventricular assist device. *Artificial Organs*, 26 (11), 947-951. https://doi.org/10.1046/j.1525-1594.2002.07125.x

[2] Masuzawa, T., Onuma, H., Kim, S.-J., Okada, Y. (2001). Magnetically suspended centrifugal blood pump with a self-bearing motor. *ASAIO Journal*, 48 (4), 437-442. https://doi.org/10.1097/00002480-200207000-00019

[3] Asama, J., Shinshi, T., Hoshi, H., Takatani, S., Shimokohbe, A. (2004). A new design for a compact centrifugal blood pump with a magnetically levitated rotor. *ASAIO Journal*, 50 (6), 550-556. https://doi.org/10.1097/01.MAT.0000144364.62671.5A

[4] Jeng, J.-T. (2000). Nonlinear adaptive inverse control for the magnetic bearing system. *Journal of Magnetism and Magnetic Materials*, 209 (1-3), 186-188. https://doi.org/10.1016/S0304-8853(99)00683-6

[5] Betschon, F., Knospe, C. R. (2001). Reducing magnetic bearing currents via gain scheduled adaptive control. *IEEE/ASME Transactions on Mechatronics*, 6 (4), 437-443. https://doi.org/10.1109/3516.974857

[6] Basaran, S., Sivrioglu, S., Zergeroglu, E. (2017). Composite adaptive control of single gimbal control moment gyroscope supported by active magnetic bearings. *Journal of Aerospace Engineering*, 30 (1). https://doi.org/10.1061/(ASCE)AS.1943-5525.0000673

[7] Su, T.-J., Li, T.-Y., Tsou, T.-Y., Giap, V.-N., Nguyen, Q.-D. (2017). Proportional–integral–derivative/fuzzy sliding mode control for suspension of active magnetic bearing system. *Advances in Mechanical Engineering*, 9 (12), 1-8. https://doi.org/10.1177/1687814017736654

[8] Zad, H. S., Khan, T. I., Lazoglu, I. (2018). Design and adaptive sliding-mode control of hybrid magnetic bearings. *IEEE Transactions on Industrial Electronics*, 65 (3), 2537-2547. https://doi.org/10.1109/tie.2017.2739682

[9] Dhyani, A., Panda, M. K., Jha, B. (2018). Moth-flame optimization-based fuzzy-PID controller for optimal control of active magnetic bearing system. *Iranian Journal of Science and Technology, Transactions of Electrical Engineering*, 42 (4), 451-463. https://doi.org/10.1007/s40998-018-0077-1

[10] Carvalho, F. C., Fernandes de Oliveira, M. V., Lara-Molina, F. A., Cavalini, Jr., A. A., Steffen, Jr., V. (2021). Fuzzy robust control applied to rotor supported by active magnetic bearing. *Journal of Vibration and Control*, 27 (7-8), 912-923. https://doi.org/10.1177/1077546320933734

[11] Humaidi, A. J., Kadhim, S. K., Gataa, A. S. (2021). Optimal adaptive magnetic suspension control of rotary impeller for artificial heart pump. *Cybernetics and Systems*, 53 (1), 141-167. https://doi.org/10.1080/01969722.2021.2008686

[12] Huettner, C. (2003). Vibration control for an implantable blood pump on a bearingless slice motor. *JSME I*nternational *Journal, Series C: Mechanical Systems, Machine Elements and Manufacturing*, 46 (3), 908-915. https://doi.org/10.1299/jsmec.46.908

[13] Ren, Z., Jahanmir, S., Heshmat, H., Hunsberger, A. Z., Walton, J. F. (2009). Design analysis and performance assessment of hybrid magnetic bearings for a rotary centrifugal blood pump. *ASAIO Journal*, 55 (4), 340-347. https://doi.org/10.1097/mat.0b013e3181a094c8

[14] Pai, C. N., Shinshi, T., Shimokohbe, A. (2010). Estimation of the radial force using a disturbance force observer for a magnetically levitated centrifugal blood pump. *Proceedings of the Institution of Mechanical Engineers, Part H: Journal of Engineering in Medicine*, 224 (7), 913-924. https://doi.org/10.1243/09544119JEIM628

[15] Da Silva, I., Horikawa, O., Cardoso, J. R., Camargo, F. A., Andrade, A. J. P., Bock, E. G. P. (2011). Single axis controlled hybrid magnetic bearing for left ventricular assist device: Hybrid core and closed magnetic circuit. *Artificial Organs*, 35 (5), 448-453. https://doi.org/10.1111/j.1525-1594.2011.01265.x

Received November 23, 2023
Accepted July 08, 2024